



# Modeling Dynamic Stall on Wind Turbine Blades Under Rotationally Augmented Flow Fields

S. Guntur and Scott Schreck  
*National Renewable Energy Laboratory*

N. N. Sørensen and L. Bergami  
*Technical University of Denmark*

**NREL is a national laboratory of the U.S. Department of Energy  
Office of Energy Efficiency & Renewable Energy  
Operated by the Alliance for Sustainable Energy, LLC**

This report is available at no cost from the National Renewable Energy Laboratory (NREL) at [www.nrel.gov/publications](http://www.nrel.gov/publications).

**Technical Report**  
NREL/TP-5000-63925  
April 2015

Contract No. DE-AC36-08GO28308

# Modeling Dynamic Stall on Wind Turbine Blades under Rotationally Augmented Flow Fields

S. Guntur and Scott Schreck  
*National Renewable Energy Laboratory*

N. N. Sørensen and L. Bergami  
*Technical University of Denmark*

Prepared under Task No. WE15.3B03

**NREL is a national laboratory of the U.S. Department of Energy  
Office of Energy Efficiency & Renewable Energy  
Operated by the Alliance for Sustainable Energy, LLC**

This report is available at no cost from the National Renewable Energy  
Laboratory (NREL) at [www.nrel.gov/publications](http://www.nrel.gov/publications).

## NOTICE

This report was prepared as an account of work sponsored by an agency of the United States government. Neither the United States government nor any agency thereof, nor any of their employees, makes any warranty, express or implied, or assumes any legal liability or responsibility for the accuracy, completeness, or usefulness of any information, apparatus, product, or process disclosed, or represents that its use would not infringe privately owned rights. Reference herein to any specific commercial product, process, or service by trade name, trademark, manufacturer, or otherwise does not necessarily constitute or imply its endorsement, recommendation, or favoring by the United States government or any agency thereof. The views and opinions of authors expressed herein do not necessarily state or reflect those of the United States government or any agency thereof.

This report is available at no cost from the National Renewable Energy Laboratory (NREL) at [www.nrel.gov/publications](http://www.nrel.gov/publications).

Available electronically at <http://www.osti.gov/scitech>

Available for a processing fee to U.S. Department of Energy and its contractors, in paper, from:

U.S. Department of Energy  
Office of Scientific and Technical Information  
P.O. Box 62  
Oak Ridge, TN 37831-0062  
phone: 865.576.8401  
fax: 865.576.5728  
email: <mailto:reports@adonis.osti.gov>

Available for sale to the public, in paper, from:

U.S. Department of Commerce  
National Technical Information Service  
5285 Port Royal Road  
Springfield, VA 22161  
phone: 800.553.6847  
fax: 703.605.6900  
email: [orders@ntis.fedworld.gov](mailto:orders@ntis.fedworld.gov)  
online ordering: <http://www.ntis.gov/help/ordermethods.aspx>

*Cover Photos: (left to right) photo by Pat Corkery, NREL 16416, photo from SunEdison, NREL 17423, photo by Pat Corkery, NREL 16560, photo by Dennis Schroeder, NREL 17613, photo by Dean Armstrong, NREL 17436, photo by Pat Corkery, NREL 17721.*

NREL prints on paper that contains recycled content.

## Acknowledgments

This work is a part of project *SYSWIND*, funded by the European Commission under the framework FP7 program *Marie Curie*. The experimental data used in this investigation were acquired from NREL's Unsteady Aerodynamics Experiment and analyzed as part of a visiting researcher collaborative activity. This part of the work was supported by the U.S. Department of Energy under Contract No. DE-AC36-08GO28308 with the National Renewable Energy Laboratory. Funding for the work was provided by the DOE Office of Energy Efficiency and Renewable Energy, Wind and Water Power Technologies Office.

## Executive Summary

It is well known that airfoils under unsteady flow conditions with a periodically varying angle of attack exhibit aerodynamic characteristics different from those under steady flow conditions, a phenomenon commonly known as dynamic stall. It is also well known that the steady aerodynamic characteristics of airfoils in the inboard region of a rotating blade differ from those under steady two-dimensional (2D) flow conditions, a phenomenon commonly known as rotational augmentation. This paper presents an investigation of these two phenomena together in the inboard parts of wind turbine blades. This analysis is carried out using data from three sources: (1) the National Renewable Energy Laboratory's Unsteady Aerodynamics Experiment Phase VI experimental data, including constant as well as continuously pitching blade conditions during axial operation, (2) data from unsteady Delayed Detached Eddy Simulations (DDES) carried out using the Technical University of Denmark's in-house flow solver Ellipsys3D, and (3) data from a simplified model based on the blade element momentum method with a dynamic stall subroutine that uses rotationally augmented steady-state polars obtained from steady Phase VI experimental sequences, instead of the traditional 2D nonrotating data. The aim of this work is twofold. First, the blade loads estimated by the DDES simulations are compared to three select cases of the N sequence experimental data, which serves as a validation of the DDES method. Results show reasonable agreement between the two data in two out of three cases studied. Second, the dynamic time series of the lift and the moment polars obtained from the experiments are compared to those from the dynamic stall subroutine that uses the rotationally augmented steady polars. This allowed the differences between the stall phenomenon on the inboard parts of harmonically pitching blades on a rotating wind turbine and the classic dynamic stall representation in 2D flow to be investigated. Results from the dynamic stall subroutine indicated a good qualitative agreement between the model and the experimental data in many cases, which suggests that the current 2D dynamic stall model as used in BEM-based aeroelastic codes may provide a reasonably accurate representation of three-dimensional rotor aerodynamics when used in combination with a robust rotational augmentation model.

# Table of Contents

<b>Acknowledgments</b> .....	<b>iii</b>
<b>Executive Summary</b> .....	<b>iv</b>
<b>Table of Contents</b> .....	<b>v</b>
<b>1 Introduction</b> .....	<b>1</b>
<b>2 Modeling Dynamic Stall</b> .....	<b>2</b>
2.1 Reduced Order Engineering Model for Dynamic Stall .....	2
<b>3 NREL Phase VI Experiment</b> .....	<b>5</b>
3.1 Determination of the AOA.....	6
<b>4 Results and Discussion</b> .....	<b>10</b>
4.1 Comparing CFD to Experimental Data .....	10
4.2 Comparing the Reduced Order Dynamic Stall Model with the Experimental Data.....	14
<b>5 Conclusion</b> .....	<b>18</b>

## List of Figures

Figure 1. The computational domain used in the present CFD simulations. The blade is visible at the center of the domain, and the inlet part of the spherical outer boundary of the domain is shown. The bottom plane shows the symmetry plane used to limit the computational domain. ....	3
Figure 2. The experimental $CL - \alpha$ curves obtained from the UAE Phase VI rotor under two different operating conditions are shown for an example case. The blue curve shows data from the rotating and pitching conditions, and the red curve shows stationary pitching conditions, both at the radial location $r/R = 0.47$ and a reduced pitching frequency of $K = 0.1$ . ....	8
Figure 3. Case N47090: The $CN$ and $CT$ as functions of the pitch angle for the case at $r/R = 0.47$ , $K = 0.1$ and a mean AOA of $\alpha_M = 8.2^\circ$ ; the error bars on the experimental data denote one standard deviation .....	9
Figure 4. Case N47350: The $CN$ and $CT$ as functions of the pitch angle for the case at $r/R = 0.47$ , $K = 0.1$ and a mean AOA of $\alpha_M = 13.5^\circ$ ; the error bars on the experimental data denote one standard deviation .....	10
Figure 5. Case N47020: The $CN$ and $CT$ as functions of the pitch angle for the case at $r/R = 0.47$ , $K = 0.0625$ and a mean AOA of $\alpha_M = 2.0^\circ$ ; the error bars on the experimental data denote one standard deviation .....	11
Figure 6. The blue dotted lines indicate the blade pitch reading as a function of time (normalized by the pitching time period) from several pitching cycles, and the vertical black lines indicate the instance at which the blade passes the tower during each pitch cycle. In (a) and (b), it is apparent that tower passage occurs at the same instance every pitching cycle, whereas in (c) this correlation is much weaker .....	12
Figure 7. Case N47180: $\alpha_M = 21.2^\circ$ , $r/R = 0.30$ , and $K = 0.036$ .....	13
Figure 8. Case N47360: $\alpha_M = 21.2^\circ$ , $r/R = 0.30$ , and $K = 0.143$ .....	13
Figure 9. Case N47170: $\alpha_M = 15.7^\circ$ , $r/R = 0.30$ , and $K = 0.036$ .....	14
Figure 10. Case N47350: $\alpha_M = 15.8^\circ$ , $r/R = 0.30$ , and $K = 0.143$ .....	15
Figure 11. Case N47240: $\alpha_M = 11.5^\circ$ , $r/R = 0.80$ , and $K = 0.024$ .....	16
Figure 12. Case N47360: $\alpha_M = 11.7^\circ$ , $r/R = 0.80$ , and $K = 0.048$ .....	17

## List of Tables

Table 1. The Values of the Parameters Reduced Frequency ( $K$ ), Mean AOA ( $\alpha_M$ ), and the Amplitude of Oscillation ( $\beta\Omega$ ) for the N Sequence Cases That Were Studied.....	4
Table 2. The Parameters $\beta\Omega$ , $K$ and the Tip Pitch for Each of the Cases Considered in Table 3 (The $K$ Value Corresponds to the Section $r/R = 0.80$ for the Cases N80220 and N80250, and $r/R = 0.95$ for the Case N95090.....)	5
Table 3. The Mean Normal Force Coefficient, $CN$ (Measured Perpendicular to the Airfoil Chord), for Selected Cases of the N and H Sequences. The Values in the Parentheses are the Percentage Difference Between the N Sequence Value and the Corresponding H Sequence Value, Defined as .....	7
Table 4. The Mean Effective AOAs, $\alpha_M$ , for Selected Cases of the N and H Sequences, Computed Using Hypothesis 1.....	7

# 1 Introduction

Dynamic stall on rotating airfoils has been studied quite extensively during the last few decades, primarily in helicopter research, see Ericsson and Reding (1988a,b); Gardner and Richter (2013); Green et al. (1992); Jumper et al. (1986); and Visbal (1991). Accurate prediction of periodic aerodynamic loads on helicopters is vital to assessing blade life, and such loads are one of the primary factors limiting the performance of these structures, see Carr (1988). In recent years, dynamic stall has also been gaining attention within wind turbine aerodynamics, see Rasmussen et al. (1999) and Schreck et al. (2001). Rotational augmentation in lift in the inboard sections is another important phenomenon that occurs on wind turbine blades, see Banks and Gadd (1963). Even though modern wind turbines are pitch regulated and do not use stall as a control mechanism, stall is unavoidable in the inner part of the blades when rated power is obtained. Coupled with turbulent inflow, yaw misalignment, and wind shear, this may give rise to dynamic stall effects in the inboard region of the blade. Both dynamic stall and rotational augmentation have received significant attention during the last few decades, but independently. Several engineering models independently model each of these two phenomenon—see, for example, Bak et al. (2006); Breton et al. (2008); and Guntur et al. (2011) on rotational augmentation, and Hansen et al. (2004); Holierhoek et al. (2013); Øye (1994); and Rasmussen et al. (1999) on dynamic stall modeling on wind turbine blades.

Most rotational augmentation models are characterized for axial operating conditions, and to the authors' knowledge, dynamic stall together with rotational augmentation in axial operating conditions has not been studied previously. The studies that looked at dynamic stall on wind turbines have pertained mostly to its operation in yawed flow [see, for example, dos Santos Pereira (2010) and Schreck et al. (2001)]. Some of the challenges that yawed conditions add to analyzing dynamic stall together with rotational augmentation were identified by Schepers (2012). In yawed flow, the induction at the rotor plane is a function of the rotor wake geometry and its influence on the induction at the given azimuthal position of the blade. Without an accurate method for quantifying the azimuthal variation in the induction caused by the skewed wake, it is difficult to define a local instantaneous angle of attack (AOA) and identify dynamic stall on a yawed turbine. The National Renewable Energy Laboratory's (NREL's) Unsteady Aerodynamics Experiment (UAE) Phase VI experimental data contains, among other signals, pressure data measured on the wind turbine blades sorted into different sequences based on its operating conditions. In the N-sequence, the rotor operates in axial conditions and the blades rotate and pitch simultaneously.

This unique data set has facilitated the study of dynamic stall together with rotational augmentation in axial operating conditions by circumventing the aforementioned challenges associated with yawed flow. Unsteady delayed detached eddy simulations (DDES) of the same rotor have also been carried out for select cases using the in-house flow solver EllipSys3D, some of which have been previously presented briefly in Guntur et al. (2013). Further, a Beddoes-Leishman-type dynamic stall model Hansen et al. (2004) was implemented for the same rotor. This work investigates dynamic stall on wind turbine blades with rotationally augmented flow fields by modeling rotational augmentation and dynamic stall separately and superimposing the results. Various N-sequence experimental data sets, the computational fluid dynamics (CFD) results, and the results from a Beddoes-Leishman-type dynamic stall model by Hansen et al. (2004) are compared and analyzed.

## 2 Modeling Dynamic Stall

Various studies have been carried out previously using CFD as well as reduced order modeling approaches in analyzing dynamic stall on rotating blades—see, for example, Leishman (2006) for an outline of some existing models. Much of this work has been within helicopter research, but several models exist that are applicable to wind turbines as well—see, for example, Hansen et al. (2004); Øye (1994); and Rasmussen et al. (1999). In this work, dynamic stall has been modeled using both unsteady CFD computations and a reduced order dynamic stall model given by Hansen et al. (2004).

### 2.1 Reduced Order Engineering Model for Dynamic Stall

The dynamic stall model by Hansen et al. (2004) is a modification of the Beddoes-Leishman dynamic stall model Leishman and Beddoes (1989) to suit wind turbine blades. The idea behind the original Beddoes-Leishman dynamic stall model is that the different physical effects influencing the aerodynamics of an oscillating airfoil can be treated as four modules: the attached flow module, the leading-edge separation module, the trailing edge separation module, and the vortex lift module. The original model was designed for helicopter rotors, which typically use thin blades and operate at high Mach numbers. In the implementation of Hansen et al. (2004), the following two modifications were made to the original model to suit wind turbine applications:

1. Most wind turbines use airfoils that are thicker than those typically used on helicopters, and leading-edge separation is less common on thick airfoils. Hence, leading-edge separation is not accounted for in this model.
2. The highest Mach numbers seen on wind turbines is only of the order of 0.3 (the speed of the tip of a blade operating at a tip speed ratio of 7 at  $U_\infty = 15$  m/s is 105 m/s), so compressibility effects are ignored.

This results in a simplified dynamic stall model that outputs time series data of dynamic lift, drag, and moment coefficients for a given input of the frequency of pitching, the mean AOA, the amplitude of oscillation, and the steady polars. The steady polars that are traditionally used as an input to this model have been 2D nonrotating airfoil data. Ideally, an accurate rotational augmentation model would be coupled with a dynamic stall model to simulate a wind turbine using BEM-based codes. Because the reliability of most rotational augmentation models is still questionable, see Guntur et al. (2011), this work uses experimentally obtained polars on rotating blades from the H, J, and N sequence data sets of the NREL Phase VI experiment as the inputs to the dynamic stall model.

#### 2.1.1 Unsteady Delayed Detached Eddy Simulations

The in-house flow solver EllipSys3D is used in all computations presented in this paper. The code is developed in cooperation between the Department of Mechanical Engineering at the Technical University of Denmark (DTU) and the former Department of Wind Energy at Risø National Laboratory, Risø-DTU [see Michelsen (1992, 1994) and Sørensen (1995)]. In the present work, turbulence is modeled by the  $k-\omega$  Shear Stress Transport (SST) eddy viscosity model Menter (1993) in the form of the DDES technique of Menter and Kuntz (2004), which is an extension of the detached eddy simulation model as proposed by Strelets (2001).

The DDES methodology is combined with the laminar/turbulent transition in the boundary layer on the blade, which is modeled with the  $\gamma$ - $\tilde{Re}_\theta$  correlation-based transition model of Menter et al. (2004)—for the present implementation, see Sørensen (2009). As the DDES methodology treats everything except the separated region using the Reynolds Averaged Navier-Stokes (RANS) methodology, the transition model can be applied in the standard way within the boundary layer.

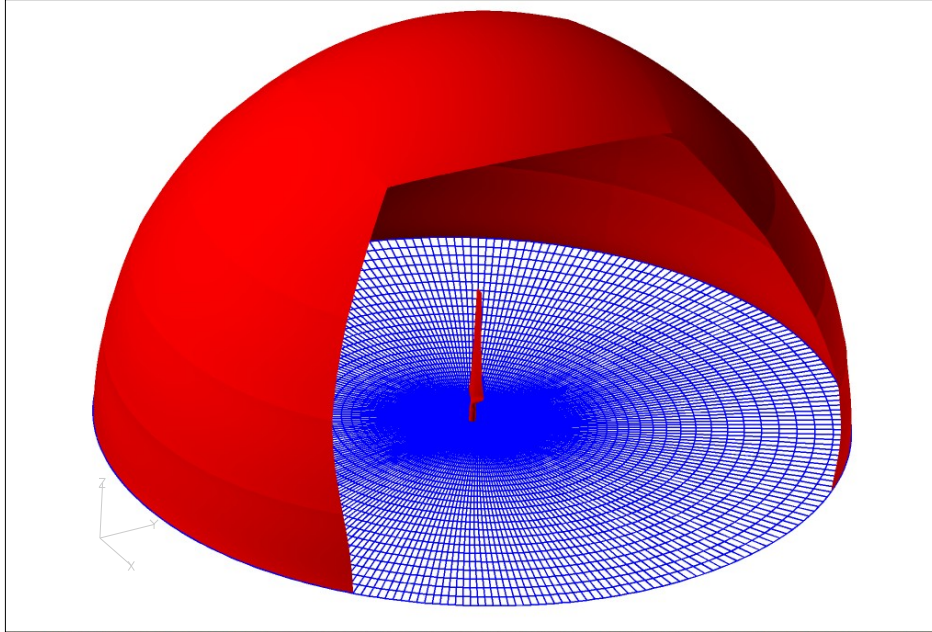


**Figure 1. The computational domain used in the present CFD simulations. The blade is visible at the center of the domain, and the inlet part of the spherical outer boundary of the domain is shown. The bottom plane shows the symmetry plane used to limit the computational domain.**

Figure 1 shows the computational domain used in the current simulations. The pitching motion of the blade is accounted for using a deforming mesh formulation in a fixed frame of reference, implemented in a generalized way to allow for an arbitrary deformation of the computational mesh. The rotational motion of the rotor is simulated by a moving mesh method, in which all the grid points in the computational mesh are moved together as a solid body, see Thomas and Lombard (1979). To ensure that no artificial mass sources are generated by the mesh deformation, the mesh velocities needed for the convective terms are computed enforcing the geometry-conservation law, as described by Ferziger (1996).

The EllipSys3D code is second-order accurate in time, using a second-order backward differencing time discretization and subiteration within each time step. In the present computation, the diffusive terms are discretized with a second-order central differencing scheme. The convective fluxes are computed using the QUICK scheme in the RANS regions, whereas a fourth-order central scheme is used for the regions in which the DDES model has switched to a large-eddy simulation technique. The simulations are computed as transient runs with 1,700 time steps per revolution and using 12 subiterations in each time step, see Sørensen and Schreck (2014). The turbulence intensity at the rotor location is controlled by the specified inflow values of the turbulent kinetic energy ' $k$ ', the specific turbulence dissipation rate  $\omega$ , and the decay of the turbulence from the inlet to the rotor location. The decay of the turbulence from the inlet to the

rotor location can be computed from the freestream velocity and the distance from the inflow boundary to the rotor location, see, for example, Langtry et al. (2006).

**Table 1. The Values of the Parameters Reduced Frequency ( $K$ ), Mean AOA ( $\alpha_M$ ), and the Amplitude of Oscillation ( $\theta_\Omega$ ) for the N Sequence Cases That Were Studied**

Case Nr.	$K$ [-] ( $r/R = 0.30$ )	$\alpha_M$ [°] ( $r/R = 0.30$ )	$K$ [-] ( $r/R = 0.47$ )	$\alpha_M$ [°] ( $r/R = 0.47$ )	$\theta_\Omega$ [°]
N47020	0.090	4.5	0.063	2.0	2.37
N47030	0.090	13.9	0.063	11.6	4.79
N47050	0.108	10.8	0.075	8.3	2.50
N47090	0.143	10.7	0.100	8.1	2.37
N47140	0.179	6.5	0.125	3.9	1.19
N47150	0.179	14.6	0.125	12.2	1.27
N47170	0.036	15.7	0.025	13.4	6.28
N47180	0.036	21.2	0.025	19.7	5.84
N47230	0.072	15.7	0.050	13.4	6.50
N47240	0.072	21.1	0.050	19.8	5.98
N47290	0.108	15.9	0.075	13.6	6.46
N47300	0.108	21.3	0.075	20.0	5.98
N47350	0.143	15.8	0.100	13.5	6.33
N47360	0.143	21.2	0.100	20.0	5.98

### 3 NREL Phase VI Experiment

NREL’s UAE Phase VI was a large-scale experiment on wind turbine aerodynamics carried out at the National Aeronautics and Space Administration’s Ames Research Center’s 80 ft × 120 ft wind tunnel. The experiment was conducted using a two-bladed 10-m-diameter turbine that was subjected to different wind speeds, pitch conditions, and rotating speeds. Pressure distributions were recorded at five locations along the blade:  $r/R = \{0.30, 0.47, 0.63, 0.80, 0.95\}$  and each location was instrumented with 23 pressure taps. The pressure distributions were used to obtain forces at these radial locations. The original experimental data were categorized into data sequences according to the operating conditions. In this work, data from four UAE Phase VI data sets are used:

1. Rotating and fixed pitch conditions (H and J sequences). Axial operation, varying  $U_\infty$ , 72 rpm, and fixed tip pitch angles of  $3^\circ$  (H sequence) and  $6^\circ$  (J sequence). Here, positive pitch is towards a decreasing AOA. The AOA on the blade was estimated using the inverse BEM method, see Guntur and Sørensen (2014a); Lindenburg (2003).
2. Rotating and pitching conditions (N sequence). Axial operation at  $U_\infty = 15$  m/s and 72 rpm, while the blade pitched continuously at various values of the reduced frequency ( $K$ ), mean pitch angle ( $\beta_M$ ), and the pitching amplitude ( $\beta_\Omega$ ). Here, the reduced frequency is defined as

$$K = \frac{\Omega c}{2U_{local}} \quad (1.1)$$

where  $\Omega$  is the pitching frequency,  $U_{local}$  is the local relative wind velocity, and  $c$  is the length of the local chord. The specific N sequence cases investigated in this work are shown in Table 1. The AOA on the blade was derived using the inverse BEM method described in the next section.

3. Parked conditions (L sequence). The rotor was parked with the instrumented blade at the 12 o’clock position, and the blade was incremented slowly in pitch. Pressure distributions at various radial locations were collected for various pitch angles, resulting in a  $C_L$  and  $C_D$  versus AOA. These data are different from typically 2D wind tunnel data in that it includes the induction caused by the trailing vortices on the blade. The AOA is taken to be the angle between the local chord and the freestream wind direction.

**Table 2. The Parameters  $\beta_\Omega$ ,  $K$  and the Tip Pitch for Each of the Cases Considered in Table 3 (The  $K$  Value Corresponds to the Section  $r/R = 0.80$  for the Cases N80220 and N80250, and  $r/R = 0.95$  for the Case N95090)**

	<i>H-seq.</i>	<i>N80220</i>	<i>N80250</i>	<i>N95090</i>
Tip pitch	$3^\circ$	$2.95^\circ$	$2.95^\circ$	$3.13^\circ$
$\beta_\Omega$	-	$10.26^\circ$	$5.79^\circ$	$2^\circ$
Local $K$	-	0.025	0.05	0.025

4. Parked pitching conditions (O sequence). The rotor was parked with the instrumented blade at the 12 o'clock position, and the blade was pitched at various values of  $K$ ,  $\beta_\Omega$ , and  $\beta_M$ . The AOA is taken to be the instantaneous angle between the local chord and the freestream wind direction.

For further details on the UAE Phase VI, see Hand et al. (2001).

### 3.1 Determination of the AOA

The assumptions and methodology adopted to estimate the AOA have been described in the previous work on the same subject, see Guntur et al. (2013). Some of it is repeated here, because it is relevant to the current work.

The normal and tangential force coefficients at the five spanwise locations,  $r/R = \{0.3, 0.47, 0.63, 0.80, 0.95\}$ , are used to estimate the induction and thereby the AOA at different sections using the inverse BEM method, see Guntur and Sørensen (2014a); Lindenburg (2003). The classical BEM theory is not capable of handling unsteady effects, which makes estimating the AOA for the N sequence data challenging. To overcome this problem, the following assumption (*Hypothesis 1*) is made: Because induction at the rotor is a far-field effect determined by the wake generated from several rotor rotations, the influence of one blade pitching cycle is negligible compared to the aggregate influence of the wake produced by several blade pitch cycles during multiple rotor rotations. In other words, the mean thrust on the flow field by the rotor blades pitching as  $\beta(t) = \beta_M + \beta_\Omega \cos \Omega t$  over a time period of  $2\pi/\Omega$  is approximately the same as a rotor operating in steady state at a constant blade pitch angle  $\beta_M$  under similar conditions. By this hypothesis, the normal force coefficients from the N sequence are averaged over one pitch cycle, and these mean forces are used as the input to the inverse BEM code. Upon obtaining a static effective AOA ( $\alpha_{eff}$ ) by this method, the dynamic effective AOA ( $\alpha_{dyn}(t)$ ) is assumed to be simply

$$\alpha_{dyn}(t) = \alpha_{eff} + \beta_\Omega \cos \Omega t \quad (1.2)$$

The reliability of the inverse BEM method for steady conditions was already validated to some extent in Guntur and Sørensen (2014a). *Hypothesis 1*, concerning unsteady conditions, was validated using the H sequence (zero yaw only) experimental series of the UAE Phase VI following the methodology documented below in connection with Tables 2 and 3. If *Hypothesis 1* is valid, then the force coefficients at different radial locations in the N sequence that also have the mean tip pitch of  $3^\circ$  must be the same as those from the H sequence, as shown below.

Table 2 shows the experimental configuration of the four sets of data that are used in the comparison presented in Table 3. As shown in Table 2, the N sequence cases N80220, N80250, and N95090 operate at mean blade tip pitch angles ( $\beta_M$ ) of  $2.95^\circ$ ,  $2.95^\circ$ , and  $3.13^\circ$ , respectively. The local  $K$  is computed as defined in Equation 1.1.

**Table 3. The Mean Normal Force Coefficient,  $C_N$  (Measured Perpendicular to the Airfoil Chord), for Selected Cases of the N and H Sequences. The Values in the Parentheses are the Percentage Difference Between the N Sequence Value and the Corresponding H Sequence Value, Defined as**

$$\epsilon = \frac{C_{N,Hseq} - C_{N,Nseq}}{C_{N,Hseq}} * 100.$$

$r/R$	<i>H-seq.</i>	<i>N80220</i>	<i>N80250</i>	<i>N95090</i>
	$C_N$	$\overline{C_N} (\epsilon)$	$\overline{C_N} (\epsilon)$	$\overline{C_N} (\epsilon)$
0.30	2.33	2.21 (5.2)	2.21 (5.3)	2.27 (2.4)
0.47	1.16	1.33 (-14.3)	1.26 (-8.3)	1.16 (0.2)
0.63	1.30	1.28 (1.6)	1.24 (4.6)	1.31 (-0.6)
0.80	0.84	1.05 (-25.3)	1.07 (-27.1)	0.90 (-7.6)
0.95	0.85	0.81 (4.4)	0.83 (2.7)	0.88 (-3.8)

**Table 4. The Mean Effective AOAs,  $\alpha_M$ , for Selected Cases of the N and H Sequences, Computed Using Hypothesis 1**

$r/R$	<i>H-seq.</i>	<i>N80220</i>	<i>N80250</i>	<i>N95090</i>
	$\alpha [^\circ]$	$\alpha_M [^\circ]$	$\alpha_M [^\circ]$	$\alpha_M [^\circ]$
0.30	28.0	28.2	28.0	27.9
0.47	28.8	28.5	28.4	28.6
0.63	24.3	24.3	24.2	24.1
0.80	21.0	20.7	20.5	20.6
0.95	18.4	18.5	18.3	18.2

In Table 3, the  $C_N$  values at the five spanwise locations for three experimental cases from the N sequence are compared to those from the H sequence. In total, 15 comparisons can be made in this table. For each  $C_N$  value, the percentage differences between the N sequence  $C_N$  values and the corresponding H sequence  $C_N$  value are shown in the parentheses. As shown, the percentage difference ( $\epsilon$ ) between the H sequence and the N sequence data is up to 27% in three cases, approximately 8% in two cases, and less than 5.3% in the remaining 10 out of the 15 cases. The higher deviations ( $\epsilon = 7.6\%$  or higher) occur at the 47% and the 80% sections.

It has been shown in Schreck (2010) and Sørensen (2009) that stall cells occur in the vicinity of the 47% section in some cases on the NREL Phase VI blade. It is a possibility that similar structures are created near the 47% and the 80% sections in the cases examined here, and these structures are responsible for the deviation seen in the four latter cases. Also, note that the first two experimental cases (N80220 and N80250) have a higher pitching amplitude,  $\beta_\Omega$ , compared to the third case (N95090), in which there is the best agreement between the averaged N sequence forces and those from the H sequence. This indicates that *Hypothesis 1* works best for low values of  $\beta_\Omega$ . Therefore, a second possibility could be that *Hypothesis 1* starts to introduce errors at high values of  $\beta_\Omega$ . Further, a third possibility could be that the lift overshoot beyond static  $C_{L,max}$  that is characteristic of classical dynamic stall is most prominent in the cases with higher  $\epsilon$  values. This lift overshoot could be because of localized transient effects that are not accounted for in the cycle-averaging procedure embraced in *Hypothesis 1*, such as stochastic perturbations caused by a tip vortex shifting in the spanwise direction that, according to Rodríguez and Theofilis (2011), may also generate stall cells at the outboard regions. These possible effects are interesting topics for future research on this subject.

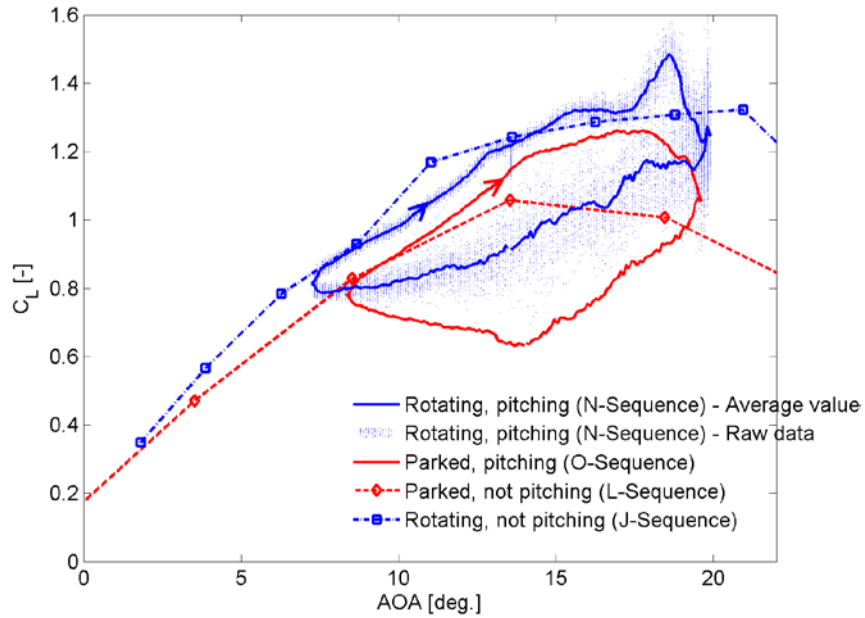


**Figure 2.** The experimental  $C_L - \alpha$  curves obtained from the UAE Phase VI rotor under two different operating conditions are shown for an example case. The blue curve shows data from the rotating and pitching conditions, and the red curve shows stationary pitching conditions, both at the radial location  $r/R = 0.47$  and a reduced pitching frequency of  $K = 0.1$ .

Overall, in a majority of shown cases there is good agreement between the H sequence and N sequence data. Because the aim here is to obtain a reliable estimate of the AOA, it is useful to analyze the error in the AOA estimates caused by a given error in the  $C_N$ . Using the inverse BEM for steady cases, the change in the estimated AOA with respect to the force coefficient,  $C_N$ , for the N sequence cases studied here has been computed as:

$$\frac{d\alpha}{dC_N} = \approx 2.73 \quad (1.3)$$

That is, for a given set of operating conditions, a change in the normal force coefficient of  $\Delta C_N = 0.2$  results in a change in the estimated local AOA of  $\Delta\alpha = 0.5^\circ$ . Even though in some cases there is a difference between the  $C_N$  from the H sequence and N sequence data sets as shown in in Table 3, the corresponding difference in the estimated local AOA between the H sequence and N sequence cases seems far less prominent. This is shown in Table 4, which shows the computed AOAs for the same cases. The differences between the estimated AOAs for the H sequence cases and the N sequence cases are negligible. Hence, *Hypothesis 1* has been deemed reasonable for carrying out the current analysis.

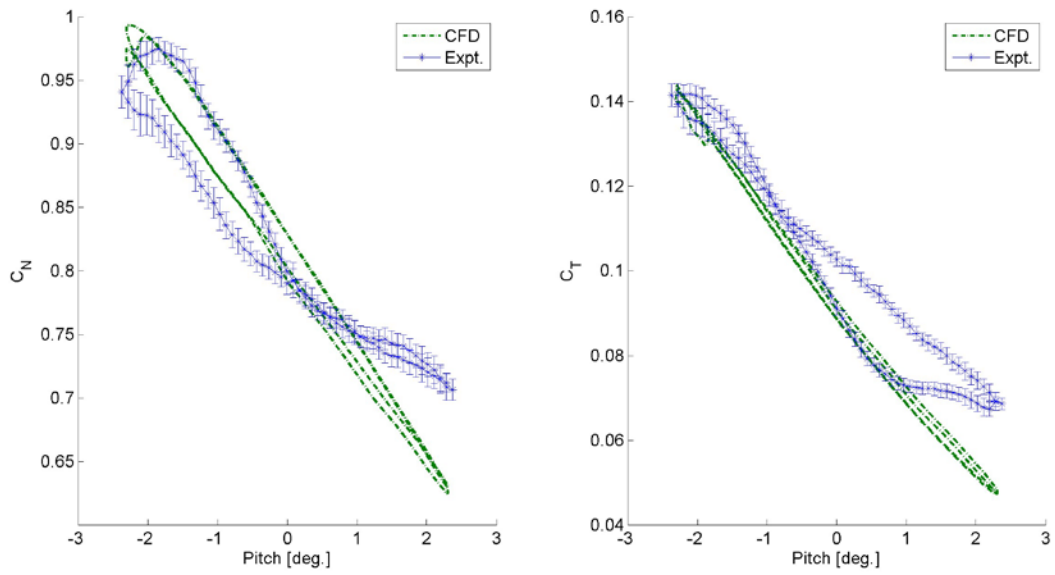


**Figure 3. Case N47090: The  $C_N$  and  $C_T$  as functions of the pitch angle for the case at  $r/R = 0.47$ ,  $K = 0.1$  and a mean AOA of  $\alpha_M = 8.2^\circ$ ; the error bars on the experimental data denote one standard deviation**

## 4 Results and Discussion

It is well known that in the inboard sections the flow field on the blade is rotationally augmented, see Herraes et al. (2014) and Schreck and Robinson (2002). Therefore, the first step in studying dynamic stall in the inboard parts of a wind turbine is to examine how lift during dynamic stall behaves in the inboard regions. Figure 2 shows the lift polars in stationary and rotating, steady and pitching conditions, obtained from the experimental data at  $r/R = 0.47$  and a reduced frequency of pitching  $K = 0.1$ . The lift curve from the steady rotating case (blue dotted line, J sequence) shows higher lift than the steady stationary case (red dotted line, L sequence), which is due to rotational augmentation. The hysteresis loop formed by the rotating and pitching case (solid blue line, N sequence) shows higher lift compared to the stationary pitching case (solid red line, O sequence), which indicates that lift in dynamic stall is proportionally augmented in rotation. Note that the area enclosed in the hysteresis loop of the N sequence is smaller than that of the O sequence. If the area within the  $C_L - \alpha$  hysteresis loop is an indication of the severity of stall on the blade, this observation is consistent with the conclusion from Guntur and Sørensen (2014b) that stall is suppressed in rotation and also that this has an effect on dynamic stall.

### 4.1 Comparing CFD to Experimental Data

Three cases—N47090, N47350, and N47020—were simulated by the unsteady DDES computational fluid dynamics computations. Forces from the CFD data were extracted at the spanwise locations where the pressure data was available from the original experiment. Figures 3, 4, and 5 show data from the cases N47090, N47350, and N47020, respectively. The normal and tangential force coefficients (measured parallel and perpendicular to the chord, respectively) shown here are at the  $r/R = 0.47$  location, obtained from the CFD simulations and the experiment. The details regarding the operating effective AOAs, reduced frequencies of pitching, and pitching amplitudes of all of the N-sequence experimental cases studied in this work are tabulated in Table 1. In the figures shown in this paper, the pitch is defined positive toward a decreasing AOA.

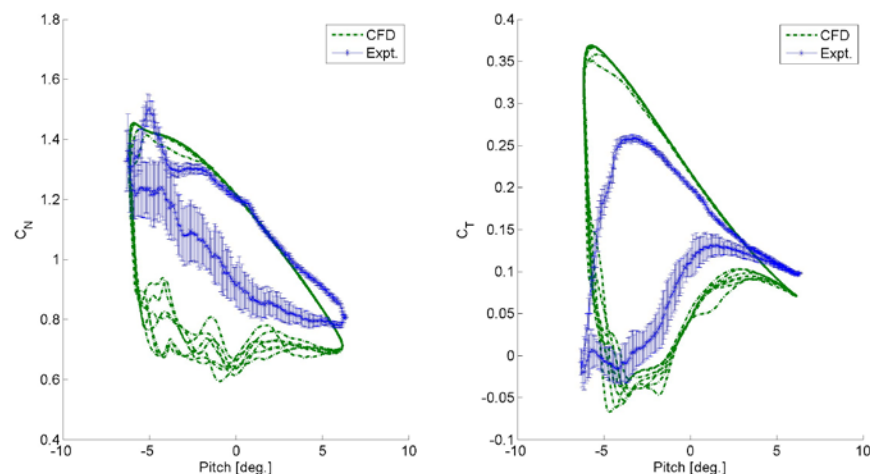


**Figure 4. Case N47350: The  $C_N$  and  $C_T$  as functions of the pitch angle for the case at  $r/R = 0.47$ ,  $K = 0.1$  and a mean AOA of  $\alpha_M = 13.5^\circ$ ; the error bars on the experimental data denote one standard deviation**

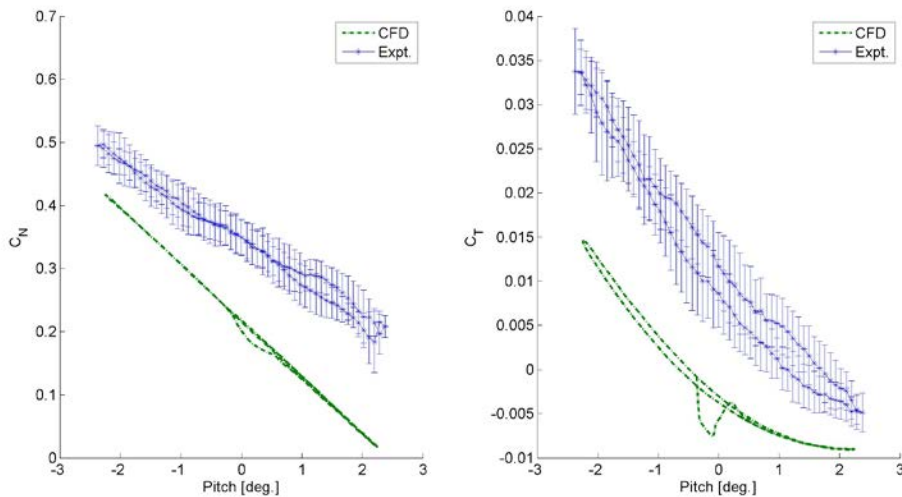


**Figure 5. Case N47020: The  $C_N$  and  $C_T$  as functions of the pitch angle for the case at  $r/R = 0.47$ ,  $K = 0.0625$  and a mean AOA of  $\alpha_M = 2.0^\circ$ ; the error bars on the experimental data denote one standard deviation**

Consider the two cases N47090 and N47350, shown in Figures 3 and 4, respectively. The case N47090 operates at a pitching amplitude of  $\beta_\Omega = 2.37^\circ$  and mean AOA of  $\alpha_M = 8.2^\circ$ . The case N47350 operates at a pitching amplitude of  $\beta_\Omega = 6.33^\circ$  and mean AOA of  $\alpha_M = 13.5^\circ$ . Both cases operate at the same pitching frequency,  $K = 0.1$ , and show good qualitative agreement between experimental and CFD data. The case N47090 shown in Figure 3 shows a good agreement between the CFD and the experimental data in  $C_N$  as well as  $C_T$ . The case N47350, which operates at a higher mean AOA of  $\alpha_M = 13.5^\circ$ , shows that there is good qualitative agreement between the two data sets, but during the reattachment phase of the dynamic stall process the CFD data predicts a more severe stall than that observed in the experiments. Sørensen and Schreck (2012) highlights that the highly unsteady and stochastic nature of flow in this region—described, for example, in Carr (1988); Ericsson and Reding (1988a,b); Visbal (1991)—makes it challenging to model using even the most advanced, state-of-the-art CFD methods. It is believed that this is one of the reasons for the observed difference between the experimental and CFD results. Further, Figures 1.6(a) and 1.6(b) show that there is a correlation between the blade pitching frequency and the rotation of the turbine in the cases N47090 and N47350. The blade passes the tower at approximately the same pitch every cycle during the decreasing part of the pitching cycle (increasing in AOA). This tower passage effect is also responsible for some of the disagreement between the CFD and the experimental data in these two cases—for example, the dip in the  $C_N$  value in Figure 3 observed at an approximate  $0^\circ$  pitch on the upper side of the  $C_N$  loop.

The third case, N47020, operates at a lower pitching frequency,  $K = 0.0625$ , and a lower mean AOA compared to the previous two cases,  $\alpha_M = 2.0^\circ$ . In Figure 5, the comparison between the  $C_N$  and  $C_T$  shows that the CFD data predicts a lower force than that obtained from the experiment. One possibility for this disagreement between the CFD and the experimental data could be that the absence of the nacelle and the tower in the CFD model gives rise to flow structures in the inboard region that are different from the experiment, which contained a nacelle and a tower. In addition, the turbine in this case operates at a tip pitch setting that is significantly different from its design configuration. The mean AOA at  $r/R = 0.47$  is approximately  $2^\circ$ , meaning that sections

further inboard have a mean AOA of slightly higher than  $2^\circ$ , and those at the outboard regions have a smaller or negative mean AOAs. This implies that there is a positive lift in the inboard region, a negative lift in the outboard region, and a zero lift region somewhere in the middle of the blade. Such a lift distribution along the blade leads to the trailing of multiple vortices along the span of the blade, in addition to the root and tip vortices. It was highlighted in Guntur and Sørensen (2014a) that a strong trailing vortex can lead to variations in the measured forces in that region. In meshing computational domains, the tip and the root region of the blades typically have more grid points enabling the tip and the root vortices to be well resolved. It is possible that these midboard trailing vortices were not modeled accurately in the present CFD computation, and that the lower lift observed in case of the CFD data is an overestimated effect of the trailing vortices. In any case, the CFD simulation in this case was not able to model the flow accurately.

Although the DDES CFD simulations were able to generate reasonable results for two out of the three cases studied (N47090 and N47350), apparently it has some limitations that restrict its accuracy in modeling the case N47020.

Further investigation is needed to analyze this discrepancy in more detail, which is outside the scope of the current study.

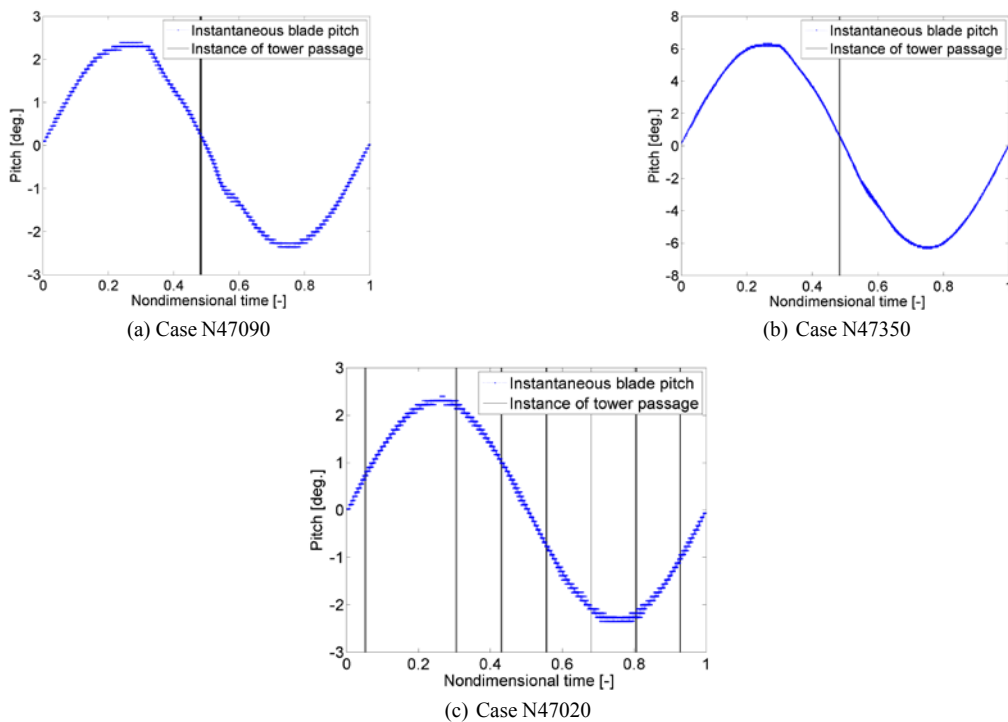


**Figure 6. The blue dotted lines indicate the blade pitch reading as a function of time (normalized by the pitching time period) from several pitching cycles, and the vertical black lines indicate the instance at which the blade passes the tower during each pitch cycle. In (a) and (b), it is apparent that tower passage occurs at the same instance every pitching cycle, whereas in (c) this correlation is much weaker**

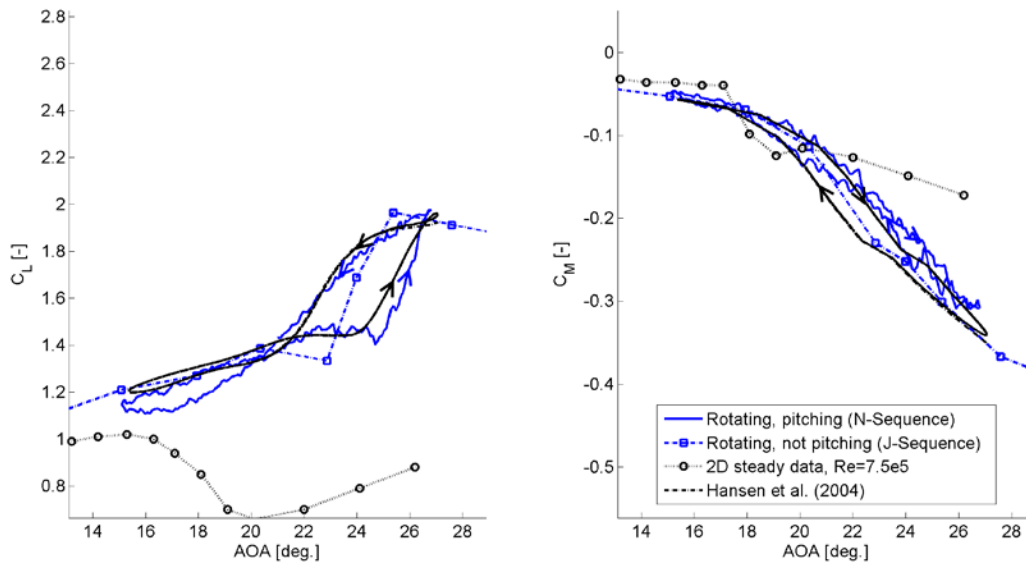


Figure 7. Case N47180:  $\alpha_M = 21.2^\circ$ ,  $r/R = 0.30$ , and  $K = 0.036$

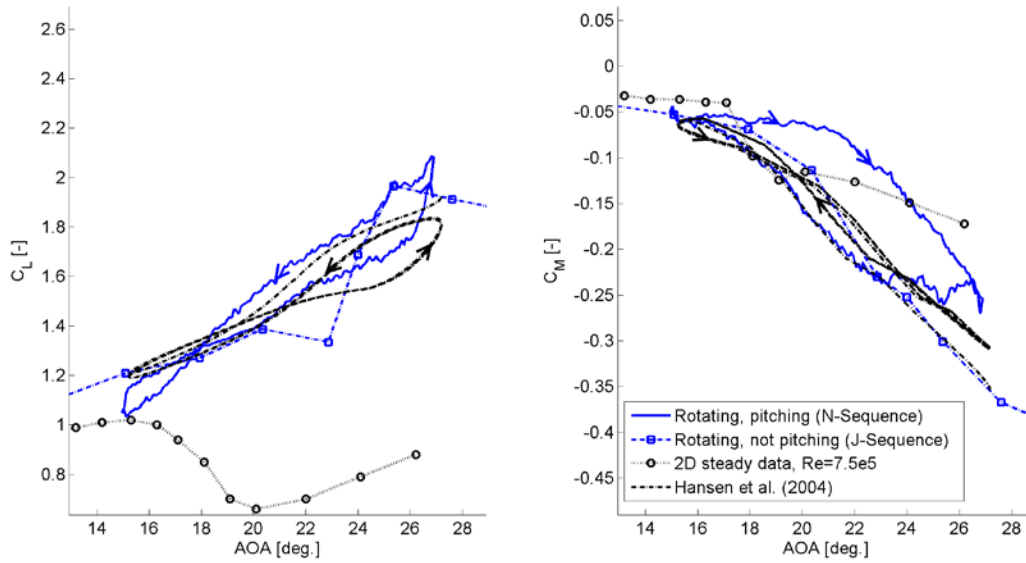


Figure 8. Case N47360:  $\alpha_M = 21.2^\circ$ ,  $r/R = 0.30$ , and  $K = 0.143$

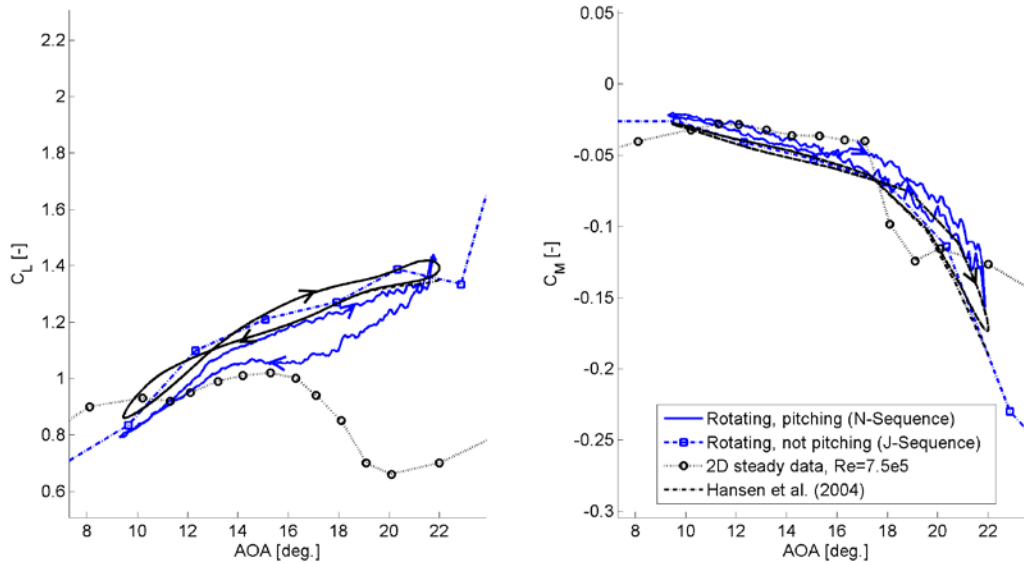


Figure 9. Case N47170:  $\alpha_M = 15.7^\circ$ ,  $r/R = 0.30$ , and  $K = 0.036$

## 4.2 Comparing the Reduced Order Dynamic Stall Model with the Experimental Data

The first two spanwise locations,  $r/R = 0.30$  and  $0.47$ , were investigated in the current work using 14 N sequence test cases. The test case numbers, and the values of the parameters  $K$ ,  $\alpha_M$ , and  $\theta_\Omega$  for these cases are shown in Table 1. In real-life wind turbines, the cyclic variation in loading under yawed operating conditions, for example, has a frequency of 1P (rotor rotation frequency), which results in a local dynamic stall reduced frequency of approximately  $K = 0.1$  in the inner parts of the rotor. The test cases chosen here operate in the ranges of  $0.036 < K < 0.18$ ,  $2^\circ < \alpha_M < 21^\circ$ , and  $1.2^\circ < \theta_\Omega < 6.5^\circ$ , which covers many cases that can occur on real wind turbines. The lift and moment polars for the selected cases are shown in Figures 7 to 12. All experimental data shown is binned and averaged over approximately 40 pitching cycles. All of the simulated data presented in this section was generated using the dynamic stall model of Hansen et al. (2004). The results from the simulation depend on the input parameters given below. Note that any uncertainties in these inputs will reflect in the output from the model:

1. The model uses the steady 3D (rotationally augmented) lift, drag, and moment polars derived from the J sequence of the Phase VI experimental data,
2. The model assumes a mean AOA as estimated by the technique described in Section 1.3.1.

Figures 7 and 8 show the lift and moment polars for the cases N47180 and N47360, respectively, at the section  $r/R = 0.30$ . The case N47180 operates at a low pitching frequency of  $K = 0.036$ , and the case N47360 operates at  $K = 0.143$ . Both of these cases operate at  $\alpha_M = 21.2^\circ$  and approximately  $\theta_\Omega = 5.9^\circ$ . Similarly, Figures 9 and 10 show a comparison between the cases N47170 and N47350, respectively. Here, too, the two figures show slow pitching  $K = 0.036$  and fast pitching  $K = 0.143$  conditions, respectively, with approximately the same amplitude of  $\beta_\Omega = 6.3^\circ$  but at a lower mean AOA of  $\alpha_M = 15.8^\circ$ .

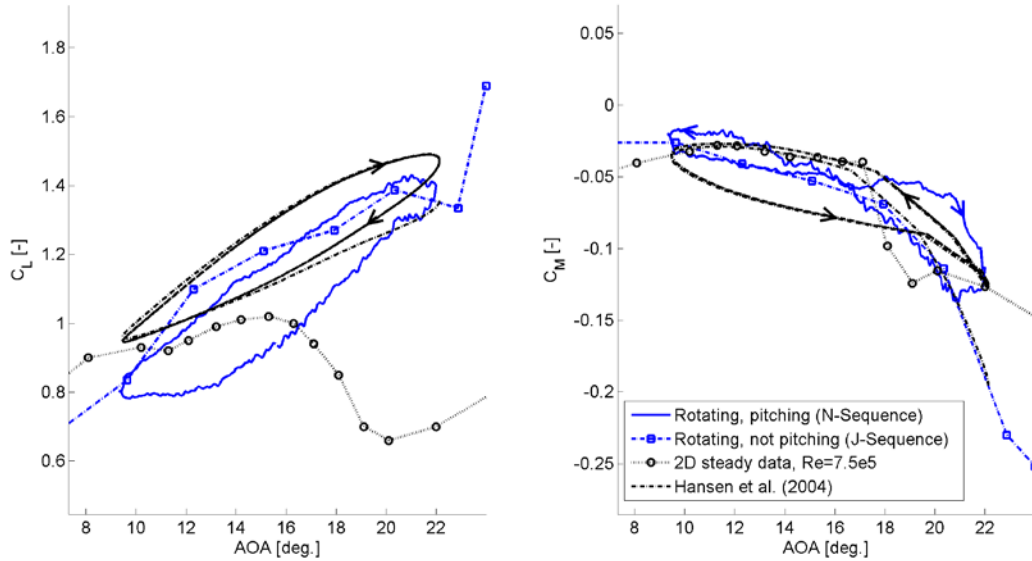


**Figure 10. Case N47350:  $\alpha_M = 15.8^\circ$ ,  $r/R = 0.30$ , and  $K = 0.143$**

Although good agreement is shown between the model and the experimental data in Figures 7 and 8, the two cases shown in Figures 9 and 10 show differences. This effect is slightly more pronounced in Figure 10, in which the difference between the mean lift values of the experimental and model data is approximately 0.17. On one hand, the mean of the unsteady experimental lift curve (solid blue line, N sequence) lies below both the steady lift curve (dashed blue line, J sequence) as well as the data from the model (dashed black curve, Hansen et al. 2004) in Figures 9 and 10. On the other hand, the areas enclosed within the  $C_L$  hysteresis loops between the experimental data and the model in Figure 10 are similar. It is also noteworthy that the experimentally obtained steady-state polar curves used here are not smooth, which may introduce some error in the model results. Given that there are uncertainties relative to post-processing of the experimental data (for example, AOA estimation in steady as well as the unsteady cases), it is difficult to conclude whether the differences observed in Figures 9 and 10 are because of experimental uncertainties, or because of the physical process itself. All in all, these four cases present a comparison among high and low pitching frequencies at high and low mean AOAs. In general, the  $C_L - \alpha$  curves obtained from the model and the experimental data show good qualitative agreement.

The hysteresis in  $C_M$  is an indication of aerodynamic damping for the pitching moment: a counterclockwise loop in the  $C_M - \alpha$  curve denotes positive damping, and vice versa. Figures 7 and 9, which show cases that operate at the same pitching frequency of  $K = 0.036$  but different mean AOAs, show a good agreement between the model  $C_M - \alpha$  data and experimental data. This shows that at this pitching frequency, the model and experiments agree well for varying mean AOAs.

Figures 8 and 10 show cases that operate at a different mean AOA and a pitching frequency of  $K = 0.143$ , which is higher compared to the previous cases in Figures 7 and 9. It is observed here that the agreement between the model and the experimental data at  $K = 0.143$  is not as good as it is at  $K = 0.036$ . In Figure 8, the experimental  $C_M$  curve shows a larger area within the  $C_M$  loop

compared to that of the model, whereas in Figure 10 the experimental  $C_M$  curve shows a smaller area enclosed within the  $C_M$  curve than that of the model. This suggests that at higher frequencies the model consistently (between the two cases shown here) predicts a more positive torsional damping.

Figures 11 and 12 show a similar comparison at the radial location  $r/R = 0.80$  at reduced pitching frequencies of  $K = 0.024$  and  $K = 0.048$ , respectively. At outboard locations, rotational augmentation effects are little to none, see Schreck and Robinson (2002), and therefore it is expected that the agreement between the dynamic stall model (which was originally developed for 2D flow fields) and the experimental data is good. Figures 11 and 12 show that although there is some agreement, there are also some specific features that can be observed in the experimental data that are not reproduced by the model. First, the model estimates separation that is less severe than what is shown by the experimental data in both figures in lift. Further, the experimental data in Figure 12 shows some peculiar behavior in lift during increasing AOA: the lift value peaks at  $\alpha = 13^\circ$ , decreases in value thereafter, and peaks again at  $\alpha = 18^\circ$  before the AOA starts to decrease. According to what is understood about dynamic stall from past literature, this behavior is unusual, and it is not exactly understood why it happens in the case shown in Figure 12.

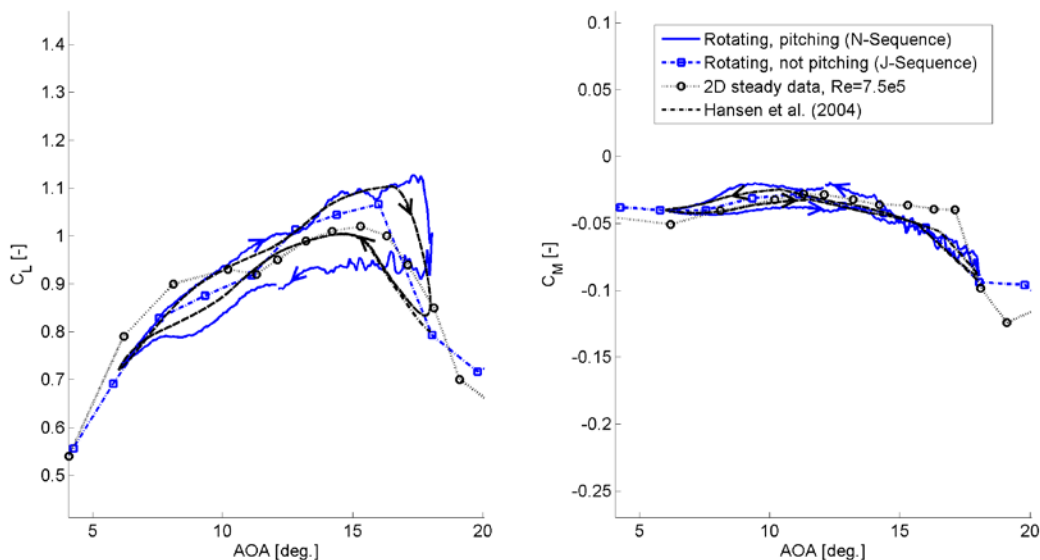


**Figure 11. Case N47240:  $\alpha_M = 11.5^\circ$ ,  $r/R = 0.80$ , and  $K = 0.024$**

As shown, the model seems to be limited in its capabilities to reproduce these specific features of lift in some cases. However, considering the uncertainties of the current approach it seems that the current model is capable of providing good qualitative estimates in both the lift and the moment in most cases and good quantitative estimates in some cases. This implies that within the range of conditions studied herein, it seems reasonable for rotational augmentation and dynamic stall to be modeled separately and be superimposed in the BEM-based aeroelastic codes. However, superposition of two strongly nonlinear phenomena across a broad parameter range entails substantial complexity and therefore uncertainty. To successfully do this across a more general range of conditions, it will be crucial to have a detailed understanding of the flow physics responsible for rotational augmentation and dynamic stall, acquired through first principles computations and detailed experiments.

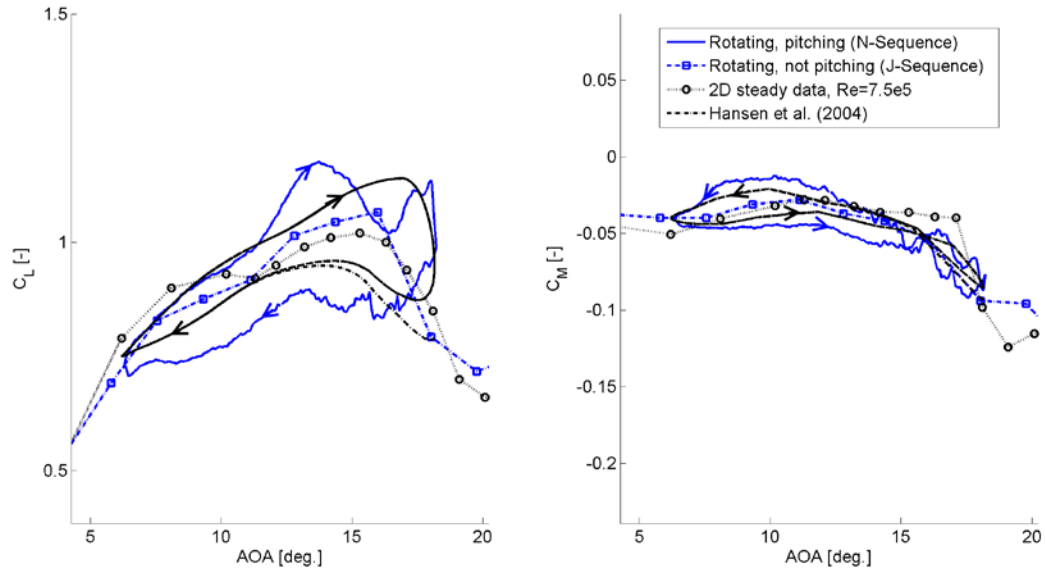


**Figure 12. Case N47360:  $\alpha_M = 11.7^\circ$ ,  $r/R = 0.80$ , and  $K = 0.048$**

## 5 Conclusion

In summary, this paper presents a study investigating dynamic stall in rotationally augmented flow fields on wind turbine blades. One of the major challenges of carrying out such a study has previously been in the ability to effectively separate these two phenomena. The present study is unique in that the distinct effects of the dynamic stall and the rotational augmentation phenomena have been analyzed separately on the inboard parts of an experimental wind turbine, the data from which inherently contains both. This study has been carried out using NREL's UAE Phase VI experimental data, which encompassed stationary and rotating blade conditions as well as fixed pitch and dynamic blade conditions.

A method for estimating the instantaneous AOA on a rotating/pitching blade using experimental data has been presented. In the experimental cases studied herein, it has been found that this method provides reliable AOA estimates. Rotationally augmented polars of the s809 airfoil used on NREL's Phase VI rotor blades have been extracted from the J sequence of the same experimental database at various radial locations, in which the turbine operates in axial, steady flow with a constant rotational speed and pitch conditions. Using the estimated AOA values and the experimentally obtained rotationally augmented polars as the input, a number of cases have been modeled using the dynamic stall model by Hansen et al. (2004) and compared to the experimental data. In some cases, certain features have been observed in the experimental data that are neither reproduced by the current dynamic stall model nor fully understood based on the current understanding of dynamic stall in the presence of three dimensionality and rotational augmentation. In the other cases, good agreement was found between the model and the experimental lift data. In analyzing the moment coefficient it was found that the model provides reasonable results at low  $K$  values and overpredicts torsional aerodynamic damping at higher  $K$  values.

Three out of the 14 N-sequence cases were modeled using unsteady DDES CFD simulations and compared to the experimental data. A qualitative agreement was found between the CFD simulations and the experimental data in two out of three cases discussed. In the third case, it was found that the CFD estimates are not in good agreement with the experimental data. It is speculated that there could be issues related to the turbine operating in conditions that are far from its design conditions. Further investigations are needed to fully understand the reasons for these disagreements.

Overall, the observations from comparing the dynamic stall model by Hansen et al. (2004) to the experimental data suggest that in some cases dynamic stall as it occurs on rotating and nonrotating blades may be similar. In the cases in which the model and the experimental data do not agree well, a more detailed understanding is needed concerning the interactions between rotational augmentation and dynamic stall, which must be gained through more high-quality computations and experiments. In any case, observations suggest that the current dynamic stall model when used along with a robust preprocessor for rotational augmentation in BEM-based aeroelastic codes can provide reasonable estimates for unsteady aerodynamic loads on wind turbines subject to constraints imposed by flow field flow physics and model physical fidelity.

## References

- Bak, C.; Johansen, J.; Andersen, P. (2006). “Three-dimensional corrections of airfoil characteristics based on pressure distributions.” *Proc. of the European Wind Energy Conference*. Athens, Greece.
- Banks, W.; Gadd, G. (1963). “Delaying effect of rotation on laminar separation.” *AIAA* 1(4); pp. 941–942.
- Breton, S.; Coton, F.; Moe, G. (2008). “A study on rotational effects and different 3D stall models using a prescribed wake vortex scheme and NREL Phase VI experiment data.” *Wind Energy* 11; pp. 459–482.
- Carr, L. (January 1988). “Progress in analysis and prediction of dynamic stall.” *Journal of aircraft* 25(1); pp. 7–17.
- dos Santos Pereira, R.B. (2010). *Validating the Beddoes-Leishman Dynamic Stall Model in the Horizontal Axis Wind Turbine Environment*. Master’s Thesis, Universidade de Lisboa. [https://dspace.ist.utl.pt/bitstream/2295/725322/1/TeseIST\\_Final.pdf](https://dspace.ist.utl.pt/bitstream/2295/725322/1/TeseIST_Final.pdf)
- Ericsson, L.E.; Reding, J.P. (1988a). “Fluid mechanics of dynamic stall part I. Unsteady flow concepts.” *Journal of Fluids and Structures* 2(1); p. 1–33.
- Ericsson, L.E.; Reding, J.P. (1988b). “Fluid mechanics of dynamic stall part II. Prediction of full scale characteristics.” *Journal of Fluids and Structures* 2(2); p. 113–143.
- Ferziger, J.H.; Peric, M. (1996). *Computational Methods for Fluid Dynamics*. Springer-Verlag.
- Gardner, A.; Richter, K. (2013). “Influence of Rotation on Dynamic Stall.” *Journal of the American Helicopter Society* 58; p. 032,001.
- Green, R.; Galbraith, R.; Niven, A. (October 1992). “Measurements of the dynamic stall vortex convection speed.” *The aeronautical journal of the royal aeronautical society* 96(958); pp. 319–325.
- Guntur, S.; Bak, C.; Sørensen, N. (2011). “Analysis of 3D Stall Models for Wind Turbine Blades Using Data from the MEXICO Experiment.” *Proc. of the 13th International Conference on Wind Engineering*. Amsterdam, the Netherlands.
- Guntur, S.; Sørensen, N.N.; Schreck, S. (July 2013). “Dynamic Stall on Rotating Airfoils: A Look at the N-Sequence Data from the NREL Phase VI Experiment.” *Key Engineering Materials* 569–570; pp. 611–619.
- Guntur, S.; Sørensen, N.N. (2014a). “An evaluation of several methods of determining the local angle of attack on wind turbine blades.” *Journal of Physics: Conference Series* 555(1); p. 012,045. doi:10.1088/1742-6596/555/1/012045
- Guntur, S.; Sørensen, N.N. (2014b). “A study on rotational augmentation using CFD analysis of flow in the inboard region of the MEXICO rotor blades.” *Wind Energy*. doi: 10.1002/we.1726

Hand, M.; Simms, D.; Fingersh, L.; Jager, D.; Cotrell, J.; Schreck, S.; Larwood, S. (December 2001). *Unsteady Aerodynamics Experiment Phase VI: Wind Tunnel Test Configurations and Available Data Campaigns*. NREL/TP-500-29955, NREL, Golden, CO, USA.

Hansen, M.; Gaunaa, M.; Madsen, H. (June 2004). *A Beddoes-Leishman type dynamic stall model in state-space and indicial formulations*. Risø-R-1354, Risø-DTU.

Herraez, I.; Stoevesandt, B.; Peinke, J. (2014). “Insight into Rotational Effects on a Wind Turbine Blade Using Navier-Stokes Computations.” *Energies* 7(10); pp. 6798–6822.

Holierhoek, J.; de Vaal, J.; van Zuijlen, A.; Bijl, H. (2013). “Comparing different dynamic stall models.” *Wind Energy* 16(1); p. 139–158.

Jumper, E.; Schreck, S.; Dimmick, R. (January 1986). “Lift-Curve Characteristics for an Airfoil Pitching at Constant Rate.” *AIAA 24th Aerospace Sciences Meeting*. AIAA-86-0117, Reno, Nevada, USA.

Langtry, R.B.; Gola, J.; Menter, F.R. (2006). Predicting 2D Airfoil and 3D Wind Turbine Rotor Performance using a Transition Model for General CFD Codes. AIAA-paper-2006-0395.

Leishman, J. (2006). *Principles of Helicopter Aerodynamics*, Chap. 9. Cambridge Aerospace, Cambridge University Press.

Leishman, J.; Beddoes, T. (1989). “A Semi-Empirical Model for Dynamic Stall.” *Journal of the American Helicopter Society* 34(3); pp. 3–17.

Lindenburg, C. (2003). *Investigation into Rotor Blade Aerodynamics: Analysis of the stationary measurements on the UAE phase-VI rotor in the NASA-Ames wind tunnel*. ECN-C-03-025, ECN, The Netherlands.

Menter, F.R. (1993). Zonal Two Equation  $k-\omega$  Turbulence Models for Aerodynamic Flows. *AIAA paper 1993-2906*.

Menter, F.R.; Kuntz, M. (2004). *The Aerodynamics of Heavy Vehicles: Trucks, Buses, and Trains*, volume 19 of *Lecture Notes in Applied and Computational Mechanics*, chapter Adaptation of Eddy-Viscosity Turbulence Models to Unsteady Separated Flow Behind Vehicles, pages 339–352. Springer.

Menter, F.R.; Langtry, R.B.; Likki, S.R.; Suzen, Y.B.; Huang, P.G.; Völker, S. (2004). A Correlation-Based Transition Model Using Local Variables, Part I - Model Formulation. In *Proceedings of ASME Turbo Expo 2004, Power for Land, Sea, and Air*, Vienna, Austria, June 14–17, 2004. ASME. GT2004-53452.

Michelsen, J.A. (December 1992). Basis3D - a Platform for Development of Multiblock PDE Solvers. Technical Report AFM 92-05, Technical University of Denmark, Department of Fluid Mechanics, Technical University of Denmark.

Michelsen, J.A. (May 1994). Block structured multigrid solution of 2D and 3D elliptic PDE's. Technical Report AFM 94-06, Technical University of Denmark, Department of Fluid Mechanics, Technical University of Denmark.

- Øye, S. (October 1994). “Dynamic stall simulated as a time lag of separation.” *Proc. of EWEC*. Thessaloniki, Greece.
- Rasmussen, F.; Petersen, J.T.; Madsen, H.A. (August 1999). “Dynamic Stall and Aerodynamic Damping.” *Journal of Solar Energy Engineering* 121(3); pp. 150–155.
- Rodríguez, D.; Theofilis, V. (2011). “On the birth of stall cells on airfoils.” *Theoretical and Computational Fluid Dynamics* 25(1-4); pp. 105–117.
- Schepers, J. (2012). *Engineering models in wind energy aerodynamics: Development, implementation and analysis using dedicated aerodynamic measurements*. Ph.D. Thesis, Technische Universiteit Delft.
- Schreck, S. (2010). “Low frequency shedding prompted by three-dimensionality under rotational augmentation.” *48th AIAA Aerospace Sciences Meeting Including the New Horizons Forum and Aerospace Exposition, January 4, 2010 - January 7, 2010*. 48th AIAA Aerospace Sciences Meeting Including the New Horizons Forum and Aerospace Exposition, American Institute of Aeronautics and Astronautics Inc.
- Schreck, S.; Robinson, M. (2002). “Rotational Augmentation of Horizontal Axis Wind Turbine Blade Aerodynamic Response.” *Wind Energy* 5; pp. 133–150.
- Schreck, S.; Robinson, M.; Hand, M.; Simms, D. (2001). “Blade dynamic stall vortex kinematics for a horizontal axis wind turbine in yawed conditions.” *J. Solar Energy Engineering* 123; pp. 272–281.
- Sørensen, N.N. (June 1995). General Purpose Flow Solver Applied to Flow Over Hills. Risø-R-827-(EN), Risø National Laboratory, Roskilde, Denmark.
- Sørensen, N.N. (2009). “CFD modelling of laminar-turbulent transition for airfoils and rotors using the  $\gamma$ - $Re_\theta$  model.” *Wind Energy* 12(8); p. 715–733.
- Sørensen, N.N.; Schreck, S. (2012). “Computation of the National Renewable Energy Laboratory Phase-VI rotor in pitch motion during standstill.” *Wind Energy* 15; pp. 425–442.
- Sørensen, N.N.; Schreck, S. (2014). “Transitional DDES computations of the NREL Phase-VI rotor in axial flow conditions.” *Journal of Physics: Conference Series* 555(1); p. 012,096. <http://stacks.iop.org/1742-6596/555/i=1/a=012096>
- Strelets, M. (2001). Detached Eddy Simulation of Massively Separated Flows. AIAA Paper 2001-0879, Russian Scientific Center “Applied Chemistry,” St. Petersburg.
- Thomas, P.D.; Lombard, C.K. (1979). “Geometric conservation law and its application to flow computations on moving grids.” *AIAA Journal* 17(10); pp. 1030–1037.
- Visbal, M. (January 1991). “On the formation and control of the dynamic stall vortex on a pitching airfoil.” *29th Aerospace Sciences Meeting*. Reno, Nevada, USA: AIAA.